Vorticity generation by the instantaneous release of energy near a reflective boundary

P. Moresco and T. E. Harris
AWE, Aldermaston, Reading RG7 4PR, United Kingdom

V. Jodoin
Oak Ridge National Laboratory, Oak Ridge, Tennessee 37831, USA
(Received 22 April 2014; published 8 August 2014)

The instantaneous release of energy in a localized area of a gas results in the formation of a low-density region and a series of shock and expansion waves. If this process occurs near a boundary, the shock reflections can interact with the density inhomogeneity, leading to the baroclinic generation of vorticity and the subsequent organization of the flow into several structures, including a vortex ring. By means of numerical simulations we illustrate the qualitative changes that occur in the pressure wave patterns and vorticity distribution as the distance from the area of energy release to the boundary is varied. Those changes are shown to be related to the combined effect of the shock waves that, respectively, initially move away and towards the center of the low-density region. In particular, we describe how for small enough offset distances the shocks internal to the inhomogeneity can make a substantial contribution to the vorticity field, influencing the circulation and characteristics of the resulting flow structures.

DOI: 10.1103/PhysRevE.90.023002 PACS number(s): 47.40.Rs, 47.40.Nm

I. INTRODUCTION

Processes such as the laser-induced ignition of combustible mixtures [1], intense explosions [2], lightning [3], and the plasma produced by particle or laser beams in the atmosphere [4,5] are often described as the instantaneous release of energy in a localized region of a gas. In some of those cases the initial conditions can be approximated by an isothermal sphere with the same density as the surrounding fluid but at a higher pressure and temperature [1,6]. The discontinuity in pressure at the surface of the sphere then generates an expanding primary shock wave and an inward propagating expansion and leads to the formation of a region of low density, or bubble, centered around the original perturbation [2,7]. The configuration considered here also contains a boundary [Fig. 1(a)], from which the primary shock generates a reflected shock that propagates in the direction of the inhomogeneity and interacts with it [Fig. 1(b)]. As described below, this interaction and the presence of additional shock waves internal to the inhomogeneity have a dominant effect on the vorticity generated in the flow, which later determines the number and characteristics of the flow structures that are formed.

The problem of the interaction of a shock wave with a localized density inhomogeneity has received ample attention because it has applications in shock-accelerated inhomogeneous flows and is relevant to numerous configurations such as in supersonic combustion [8], inertial confinement fusion [9], and most generally to those cases where shock-induced instability plays a central role in the generation of turbulence and mixing (see [10] for a review). The problem considered here presents peculiar characteristics because of the mechanisms generating the bubble and shock. The main shock interacting with the bubble originates in the inhomogeneity itself and shares with it its spherical geometry. This introduces a dependence for the shock strength and its angle of incidence at the time of the interaction that is different from the more widely studied case of planar shock waves. Also, shortly after the appearance of the primary shock, a second shock is formed between the contact surface marking the boundary of the bubble and the tail of the internal expansion [11]. This shock wave first propagates inward, increasing rapidly in strength as it converges and reflects at the center of the bubble. When it later reaches the density interface, it is refracted and generates a third shock, which propagates towards the bubble center, and a transmitted shock wave moving in the same direction as the primary shock. The successive repetition of this process results in a series of ancillary shocks of decreasing intensity that emanate from the bubble. The presence of these waves makes the density and entropy distributions inside the bubble nonuniform and time dependent, differing from what we will call the standard shock-bubble interaction problem. In that case the inhomogeneities initially have uniform temperature and density and are in thermal and mechanical equilibrium with the surrounding gas [10]. In our case the combined effect of the reflected and ancillary shocks results in a flow circulation that depends on the distance to the boundary [denoted by H in Fig. 1(a)] in a nonmonotonic way, even though the strength of the reflected shock interacting with the bubble continuously increases as H is reduced. Although the effects of the ancillary shocks on the vorticity field have been considered in the past, it was mainly for configurations where their contribution was relatively small [12]. Our intention in this work is to illustrate that the outcome can be substantially different if boundaries are present in the proximity of the point where the energy is released.

The analysis presented is based on the numerical calculations obtained with the scheme briefly described in Sec. II, where we also give further details of the configuration and approximations involved. Results will be shown for four values of H that were found to be representative of the changes that occur as the distance to the boundary is varied. The wave patterns arising from the interaction of the shock waves with the reflective boundary and bubble are described in Sec. III. It is shown that the mutual effects of the reflected and ancillary shocks can result in reflection and refraction patterns

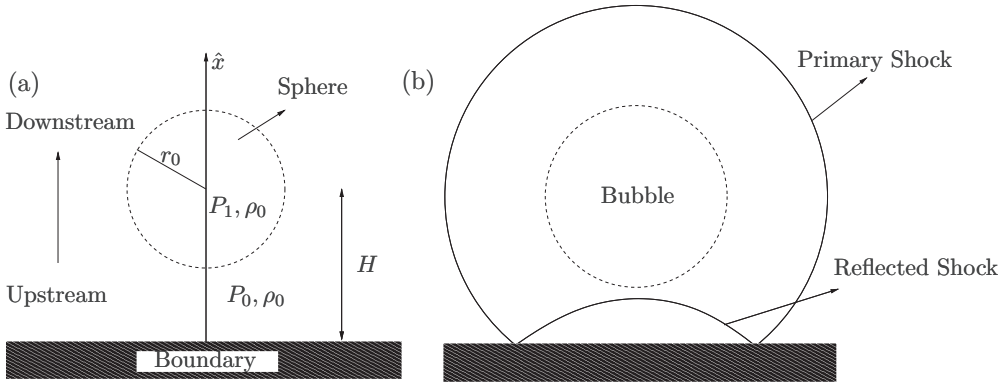

FIG. 1. (a) Cross section of the initial configuration. (b) Schematic representation of the primary and reflected shock waves.

that are sensitive to the value of H. In Sec. IV we present the development of the bubble into several flow structures, including vortex rings, and we discuss the variation in their dimensions and motion. The calculated vorticity fields are shown in Sec. V and are interpreted in terms of the interaction of the bubble with the different shock waves, allowing us to explain the differences in flow evolution as H is varied.

II. NUMERICAL SCHEME

In the computations presented here the effects of molecular dissociation and ionization were not considered. We also neglected thermal conduction and radiation, as in most applications the associated time scales will be much larger than those corresponding to the processes described here. The system studied consisted of a one-component ideal gas with a ratio of specific heats of 1.4, which was taken to be constant. We also have assumed that the time scales involved were so short that viscous and gravitational effects could be ignored. Although these assumptions are likely to be invalid in many practical cases, we believe the quantitative differences they introduce do not affect significantly the characteristics of the flow we describe here, as previous numerical and experimental studies of similar configurations indicate [6,13]. The problem was formulated in terms of the compressible Euler equations and written in conservative form for the mass, momentum, and energy in the gas [14]. Solutions to these equations were obtained by means of the one-dimensional monotonic upstream-centered scheme for conservation laws–Hancock finite-volume scheme [15], using a Harten–Lax–van Leer–contact Riemann solver and a monotonized central limiter [14]. This approach, which gives second-order accuracy in space and time and good resolution of shock waves with low numerical dissipation, was extended to three dimensions using Strang splitting [16].

The initial configuration resulting from the instantaneous release of energy was taken to be in the form of a uniform spherical region with higher pressure and temperature than the surrounding gas [Fig. 1(a)]. The equations of motion were nondimensionalized using the radius of the sphere r_0, the pressure P_0, and density ρ_0 of the unperturbed gas, whose speed of sound c_0 was used to express the unit of time as r_0/c_0. Simulations were set in three dimensions, as numerical studies [12,17] have shown that important features are not captured in two-dimensional calculations. A uniform Cartesian grid was used and zeroth-order transmissibility boundary conditions were implemented on the surface of the domain, except along the reflective boundary where infinite acoustic impedance and free-slip conditions were applied. The representation of the initial spherical bubble in a Cartesian grid introduces asymmetric grid-scale perturbations, which can later be amplified by instabilities in the flow, making it three dimensional. The computational domain used measured $20r_0$ in each direction, with the sphere centered in the plane parallel to the boundary.

The spatial resolution of the results presented here was chosen based on the requirement that the large-scale features of the flow relevant to this work did not show substantial variation with further refinement of the numerical grid. We have taken into account both the number of flow structures and their dimensions as points of comparison. As an example of this, Fig. 2 shows two important parameters for the flow evolution: the time required for the bubble to roll up into a vortex ring (cf. Sec. IV) and the distance along the axis $\hat{x}$ between the upstream and downstream portions of the density interface [see Fig. 1(a) for the adopted upstream-downstream directions] at a given nondimensional time τ (equal to 27 in this case). These results correspond to $H = 2$, which, among the parameter values considered, shows the most variety in flow structures during the roll-up of the bubble. The spatial resolution in Fig. 2

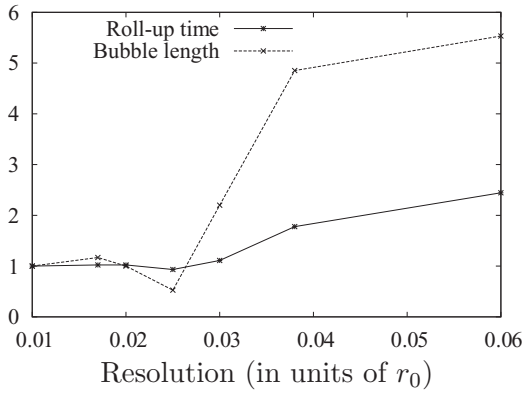

FIG. 2. Variation of roll-up time and bubble length (in the upstream-downstream direction) as a function of the grid resolution for $H = 2$ and $\tau = 27$.

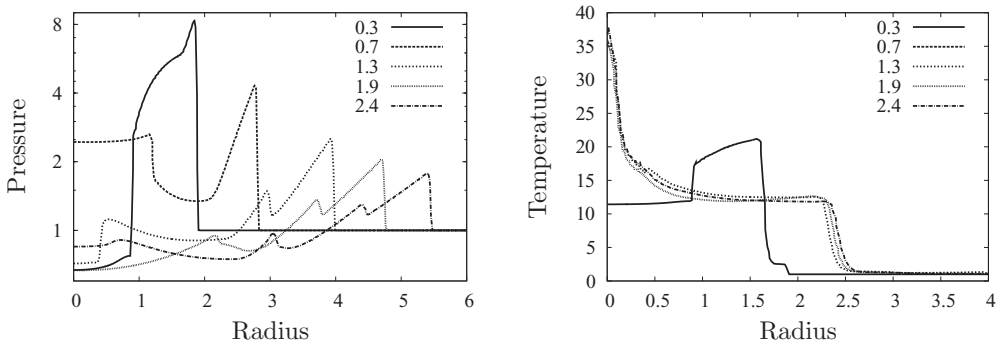

FIG. 3. Examples of the radial distributions of (a) pressure and (b) temperature centered around the bubble, in the absence of the solid boundary. Different curves correspond to different times.

is given in units of r_0 and the measured values are normalized with respect to those for a $0.01r_0$ resolution. From these and similar quantitative results, it was decided that a resolution of $0.02r_0$ was an adequate balance between numerical costs and accuracy of the solutions given the available computational resources and it has been used for the results presented here. As it has been previously described [18], there are indications that the solution of the initial-value problem for the compressible Euler equations in the presence of vortex sheets will not converge when obtained with the numerical methods used here. It can then be expected that the small-scale features resulting from the shock-bubble interaction will continue changing as the resolution is increased. Nevertheless, we believe that those variations will not qualitatively change the functional dependence of the flow characteristics with H, which are the subject of this work.

Initially the gas was defined as quiescent and inside the sphere the density was considered to be uniform and equal to ρ_0, while the pressure was defined as $P_1 = 35P_0$. This pressure ratio is an independent parameter in this configuration and different values will change the scalings in the problem and the values of H at which transitions to different regimes are observed. Results are presented below for four values of H, namely, 4, 3, 2.4, and 2, which were found to be representative of the principal changes in the flow pattern and vorticity distribution as H is varied.

III. EVOLUTION OF SHOCK WAVES AND THEIR INTERACTION WITH THE BUBBLE

As the primary shock wave moves ahead of the bubble surface, a rarefaction expands towards its center and leads to the formation of a region of low density around the original perturbation. For this type of configuration it has been shown [19,20] that in spherical and cylindrical geometries the dependence of the volume differential on the radius results in a pressure at the tail of the rarefaction that is lower than that behind the expanding shock, leading to a pressure discontinuity and the formation of an extra shock. This second shock is the first in a series of ancillary shocks that have been observed in numerical simulations, for example, of detonation of high explosives [21], the development of "hot channels" [12], and experimentally in the sudden release of high-pressure gas spheres [22,23]. Since the characteristics of the reflection of the primary shock along the boundary have been described in the past [24,25], the main focus here is going to be on the interaction of the reflected shock with the bubble and the contribution of the ancillary shocks to the wave patterns.

In the absence of the external boundary, the spherical symmetry of the initial configuration would be preserved at early time and examples of the calculated radial distributions of pressure and temperature as a function of time are shown in Fig. 3. For $\tau = 0.3$ the primary shock can be seen moving away from the bubble, while the second shock converges towards its center. At time $\tau = 0.7$ the second shock has already reflected off the center, leaving around it a region of high temperature or core. In Fig. 3(b) the large temperature gradients at the bubble surface and core can be seen. The inward propagating third shock and the diverging second and primary shocks are shown in Fig. 3(a) for $\tau = 1.3$. The refraction of the third shock at the bubble surface occurs at $\tau = 1.9$ and thereafter a fourth compression wave appears that can be seen propagating towards the center of the bubble for $\tau = 2.4$. The high temperature at the core shows maxima of decreasing amplitude with the passage of the successive ancillary shocks. For all the values of H considered, steep temperature and density gradients remained in that region during the time of the interaction between the reflected shock and the bubble. The presence of the core is one of the distinctive features of the problem considered here in comparison with the standard shock-bubble interaction and it will be shown in Sec. IV that it leads to the formation at later time of an additional vortex ring. The radial positions in time of the primary and ancillary shock waves, as well as that of the contact surface, are shown for the free-space configuration in Fig. 4, where it is easy to visualize the successive generation of the ancillary waves following their refraction at the bubble surface. When the release of energy occurs near a reflective boundary, eventually the reflected shock will interact with the surface of the bubble. There it will be refracted because of the mismatch in acoustic impedances on both sides of the interface, resulting in the formation of a transmitted shock and complex pattern of additional waves and contact surfaces. From this time onward the bubble loses its spherical symmetry and the development of the ancillary shocks and the interface will depart from that presented in Fig. 4.

The initial refraction of the reflected shock at the bubble surface is of the slow-fast type, with the wave transmitted

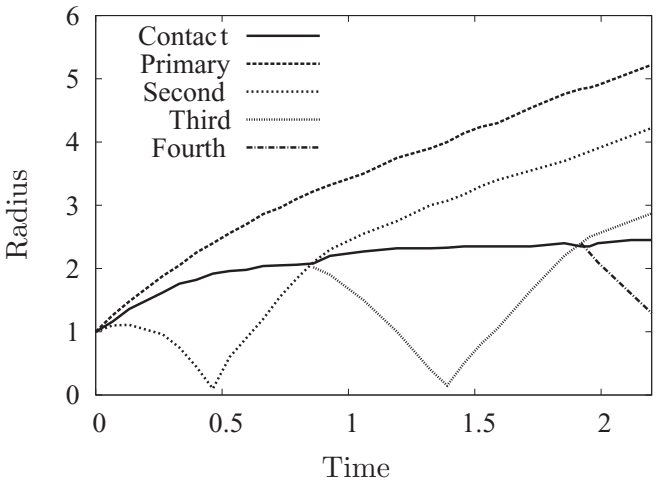

FIG. 4. Radial position with time of the contact surface and the primary and ancillary shocks.

into the bubble moving at higher speed than the incident wave [17,26]. The parameters that affect the refraction of a shock at an interface are the angle of incidence, the strength of the shock, and the material properties [27,28]. The equations describing the refraction process present singular behavior at certain parameter values that mark the transition between different patterns [27]. We can then expect that variations in the initial location of the bubble with respect to the boundary, and the effect this has on those parameters, will result in important changes in the observed characteristics of the refraction process and the subsequent flow evolution.

Several studies have been concerned with the interaction of planar shock waves with planar material interfaces. They have looked at the refraction patterns for a discrete number of shock strengths and angles of incidence, as well as various material configurations [26,29]. It has been shown that for small angles of incidence α_i, the configuration corresponds to a regular refraction, where the incident i, transmitted t, and reflected r waves meet at a point on the interface [Fig. 5(a)]. In the slow-fast configuration, t is a shock and r an expansion and with increasing α_i, a critical value is reached where the regular refraction configuration ceases to be compatible with the boundary conditions at the waves and interface and an irregular refraction pattern takes its place. In fact, for larger α_i several critical angles can be determined that describe transitions between different irregular configurations [29]. The order in which these occur and the angular ranges for which they are valid depend on the characteristics of the media involved and the strength of the incident shock. Although several irregular wave configurations have been identified for slow-fast interfaces, in simplified form they can be classified on the basis of the strength of the incident shock as the weak or strong type (Fig. 5) because of the parallels they present with the classification of irregular patterns in shock reflections [26,29,30]. In our case, the interface and the shock front are curved and the angle of incidence and consequently the nature of the refraction process change as the reflected shock expands and the contact point moves along the surface of the bubble.

In Fig. 6 details of the shock and bubble interaction patterns are shown for decreasing values of H. The continuous lines are isobars in logarithmic scale, while the noncontinuous lines are isotherms used to demarcate the surface of the bubble (denoted by C in some of the figures). In Fig. 6(a1) ($H = 4$) we have indicated the primary (P) and reflected (R) shocks, the transmitted shock (t), and the expansion (r) reflected from the bubble surface. This configuration corresponds to a regular shock refraction, which is also observed at the beginning of the shock-bubble interaction for the other values of H. Also visible are two other shocks following the primary shock, which are the second (SS) and third (T) shocks, that have left the bubble at times $\tau = 0.9$ and 1.8, respectively, before the reflected shock reached the interface at $\tau = 2.5$. In the region between the reflected shock and the boundary, several new waves and contact surfaces appear from the interaction between the reflected shock with the second and third shocks, and their respective reflections from the boundary. As the reflected shock continues its interaction with the bubble and the angle of incidence increases, a transition to a weak type of irregular refraction configuration occurs. The transmitted wave now moves ahead of i and r along the interface, becoming a precursor [Fig. 5(b)]. The fast-slow refraction of t at the interface gives place to the evanescent wave s outside the bubble. This wave interacts with i (and subsequently with r) and forms the shock k, as shown schematically in Fig. 5(b). This transition can be seen in Fig. 6(a2), where the different waves are identified. The resulting configuration has similar characteristics to the free precursor von Neumann refraction pattern observed by Henderson *et al.* [26,30] for the slow-fast refraction of weak shocks.

In the case $H = 3$, the reflected shock reaches the interface at $\tau = 1.2$, after the second shock but before the third shock has left the bubble. Now, as time progresses and because of the higher strength of the reflected shock, the regular refraction

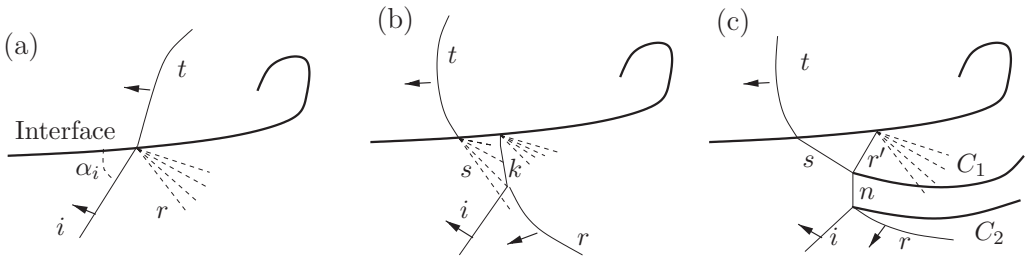

FIG. 5. Schematic representation of the (a) regular, (b) weak irregular, and (c) strong irregular refraction patterns.

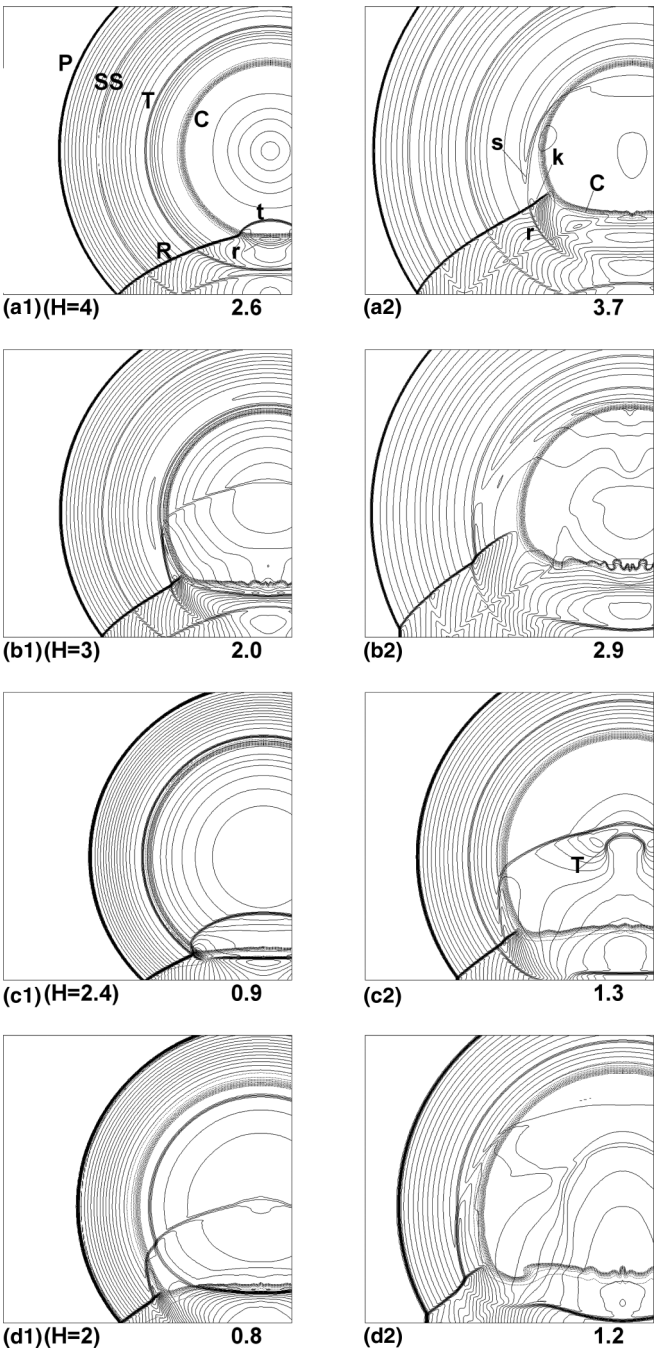

FIG. 6. Details of the pressure field around the bubble depicted with isobars on a logarithmic scale. The rows (a)–(d) correspond to H equal to 4, 3, 2.4, and 2, respectively. The time of each plot is indicated in the lower right corner.

pattern evolves into the strong irregular configuration shown in Figs. 6(b1) and 7, and schematically in Fig. 5(c), where the wave s is a shock and n is a Mach stem. From the interaction of s with n, a wave r' appears and its reflection off the bubble surface results in an expansion. In this configuration there are two triple points and associated contact surfaces [C_1 and C_2 in Fig. 5(c)] and it bears similarities to the twin Mach reflection-refraction pattern observed by Henderson *et al.* [26] for strong shocks. When the third shock leaves the bubble ($\tau = 1.9$) and later reaches this refraction pattern, it strengthens the

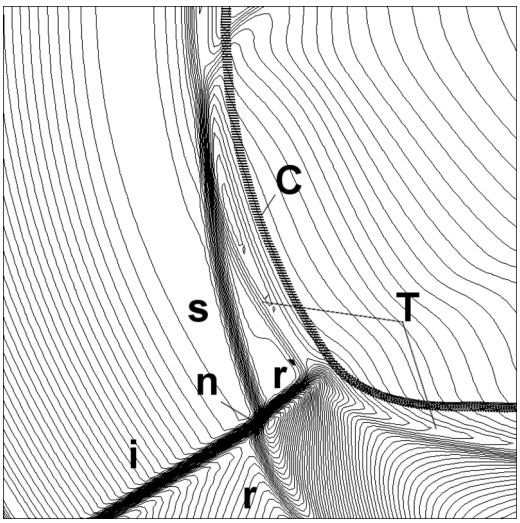

FIG. 7. Detail of the irregular shock refraction pattern in Fig. 6(b1).

different waves and makes them more inclined towards the flow [Fig. 6(b2)]. For $H = 2.4$, the second shock reaches the upstream portion of the interface after it has been deformed by the reflected shock in a regular refraction configuration [Fig. 6(c1)]. At later times the irregular refraction pattern that emerges is similar to that seen for $H = 3$, but with the reflected wave r having merged with the second shock [Fig. 6(c2)]. For $H = 2$, the reflected shock wave reaches the surface of the bubble at $\tau = 0.4$ and a transition to a strong irregular refraction pattern occurs before the second shock has gone through the interface. At a later time, the second shock catches up with the external twin Mach reflection-refraction configuration [Fig. 6(d2)], strengthening it and eventually (not shown) leading to the merger of the n wave with the Mach stem in contact with the boundary (originating from the irregular reflection of the primary shock).

The evolution of the transmitted shock after the transition to an irregular refraction pattern is similar in all the cases considered. When this wave reaches the core of the bubble, a further refraction process occurs [e.g., Fig. 6(d1)], although the shock strengths and the magnitude of the density gradients involved are lower. Later, when the transmitted shock arrives at the downstream surface of the bubble, a weak shock wave is reflected (as this is a fast-slow type of refraction), which is focused and later diverges, propagating in the upstream direction and producing further reflections and waves with decaying intensity. As the third and consecutive ancillary shocks originate in reflections from the bubble surface, they cease to be spherical after this interface has been deformed by the reflected shock. This loss of radial symmetry is compounded by the changes in gas conditions inside the bubble after the passage of the transmitted shock and the waves derived from it. This causes different parts of these ancillary waves to travel at different speeds and to converge as curved fronts towards the center of the bubble, where they are also refracted at the core. Examples of the asymmetric third shock (labeled T) converging near the center of the bubble can be seen in Figs. 6(c2) and 6(d2).

IV. BUBBLE EVOLUTION

The complex pattern of shocks, expansions, and contact surfaces described above is a general feature of the scattering of a shock wave by a bubble [31,32]. As a consequence of this interaction, vorticity is generated on the bubble surface by the baroclinic mechanism, but it can also be produced in the rest of the flow because of the curvature of the shock fronts, the nonuniformity of conditions in the fluid, and the presence of triple points and the associated contact discontinuities and shear layers [33]. In our case, with a higher speed of sound and lower acoustic impedance inside the bubble, the configuration is usually described in the literature as the interaction of a shock wave with a light or divergent bubble [10,31,34]. It has been found in experimental and numerical studies of the standard shock-bubble problem that, during its interaction with the shock, the inhomogeneity is compressed and accelerated in the direction of shock propagation and at least one vortex ring is formed following the roll-up of the unstable shear layer on the bubble surface [10]. Several approximate analytical models have been proposed that predict the velocity and circulation of this vortex ring with a varying degree of success [17], but they rely on important simplifying assumptions about the distribution of baroclinically generated vorticity on the surface of the bubble [10,17]. As shown below, the use of these approximations for the configuration considered here is limited because of the more complex vorticity field and its sensitivity to variations in the offset distance H from the bubble to the boundary.

In Fig. 8 we used isothermal curves as a way of visualizing the evolution of the bubble with time. The figures are slices of the three-dimensional results containing the initial axis of symmetry [marked $\hat{x}$ in Fig. 1(a)], with the reflecting boundary located at the bottom, i.e., in a similar configuration to that in Fig. 1. At the earliest time shown for each H (the first column) the transmitted shock has already completed its transit through the bubble and clearly visible are the deformed bubble surface and core. The figures in the second column correspond approximately to the time at which the upstream section of the bubble surface impinged on the downstream part of the interface. The other times in Fig. 8 were chosen to better illustrate important changes in the characteristics of the bubble. In the case $H = 4$ [Fig. 8(a)], the evolution has similar characteristics to that observed experimentally and numerically by Ranjan *et al.* [35] when they studied the interaction of a helium bubble in air with a planar shock wave with Mach number 1.45. As described there, vorticity is generated baroclinically over the surface of the bubble from the interaction of the local density gradient and the pressure gradient at the shock front, making the density interface elongate in the direction of the shock propagation and roll up into a kidney shape. Two main structures emerge at later time: the one downstream [upper part of Fig. 8(a4)] containing a minority fraction of the mass of the bubble, the remainder of which is located upstream in a lobelike structure [labeled L in Fig. 8(a4)]. In our case two vortex rings with circulation of the same sign but different intensity are contained in the downstream structure. We denote these as primary and secondary rings, respectively, indicated by P and S in Fig. 8(a4). For this value of H we found that the downstream structure propagates away from the boundary, while the lobe remains practically stationary. In all the cases considered here, most of the mass in the downstream structure and the highest proportion of the vorticity generated on the bubble surface are contained in the primary vortex ring, which plays the same role as the main vortex ring described in the standard shock-bubble interaction problem. On the other hand, we found that the vorticity and mass around the core of the bubble are responsible for the formation of the secondary vortex ring.

For $H = 3$ [Fig. 8(b)], the early evolution of the interface parallels that for $H = 4$, but differs at later time when the two main distinct structures are formed. In this case the evolution is congruent with that found in the experiments by Ranjan *et al.* [35] for a shock wave with Mach number 2.08. The distribution of bubble mass is substantially altered from the case $H = 4$, with most of it now contained in the downstream structure, which is connected to the lobe by a region of bubble material or strand [shown as B in Fig. 8(b4)]. A similar redistribution of bubble mass has been observed in experimental studies of the standard shock-bubble problem [35,36] for increasing Mach number of the incident shock and in our case this is compatible with the higher strength of the reflected shock as H is reduced. It can also be seen in Fig. 8 that for $H = 3$ and lower [Figs. 8(b)–8(d)], the flow becomes increasingly asymmetrical and the more complex pattern of the isotherms indicates an enhanced entrainment of the surrounding gas by the bubble. In terms of the distribution of bubble mass, the same trend continues for $H = 2.4$, with almost all of the mass now contained in the primary vortex ring, the upstream structure having almost disappeared [Fig. 8(c4)]. Now the velocity of propagation of the primary vortex ring has decreased substantially, which will be shown to be caused by a marked reduction in its circulation. The velocity of propagation of the second vortex ring is not affected in the same way, which leads to a larger separation from the primary ring [Fig. 8(c4)].

An important change in the bubble evolution is shown in Fig. 8(d) for $H = 2$. As for larger values of H, the interaction with the reflected shock results in the initial flattening of the upstream part of the bubble surface, but in this case this part of the interface is seen later to protrude towards the boundary [Fig. 8(d1)]. Eventually a region of bubble material separates from the rest [Fig. 8(d2)] and forms a stem [marked by T in Fig. 8(d3)]. At later time, reversing the trend seen for larger H, there is an increase in the proportion of bubble mass contained in the upstream structure [Fig. 8(d4)]. The secondary vortex ring is now found to move towards the boundary, indicating a change in the sign of its circulation, and the primary vortex ring presents a more clearly defined core and a higher propagation speed than in the $H = 2.4$ case.

V. VORTICITY DISTRIBUTION

We now relate the characteristics of the vorticity field to the bubble evolution described in Sec. IV. Figure 9 shows the vorticity fields for the same parameter values considered in Fig. 8. The plots show the azimuthal component of the vorticity (in the direction perpendicular to the figures), with different skewed scales used in each case to emphasize its positive (light) and negative (dark) sign distributions. At the first point

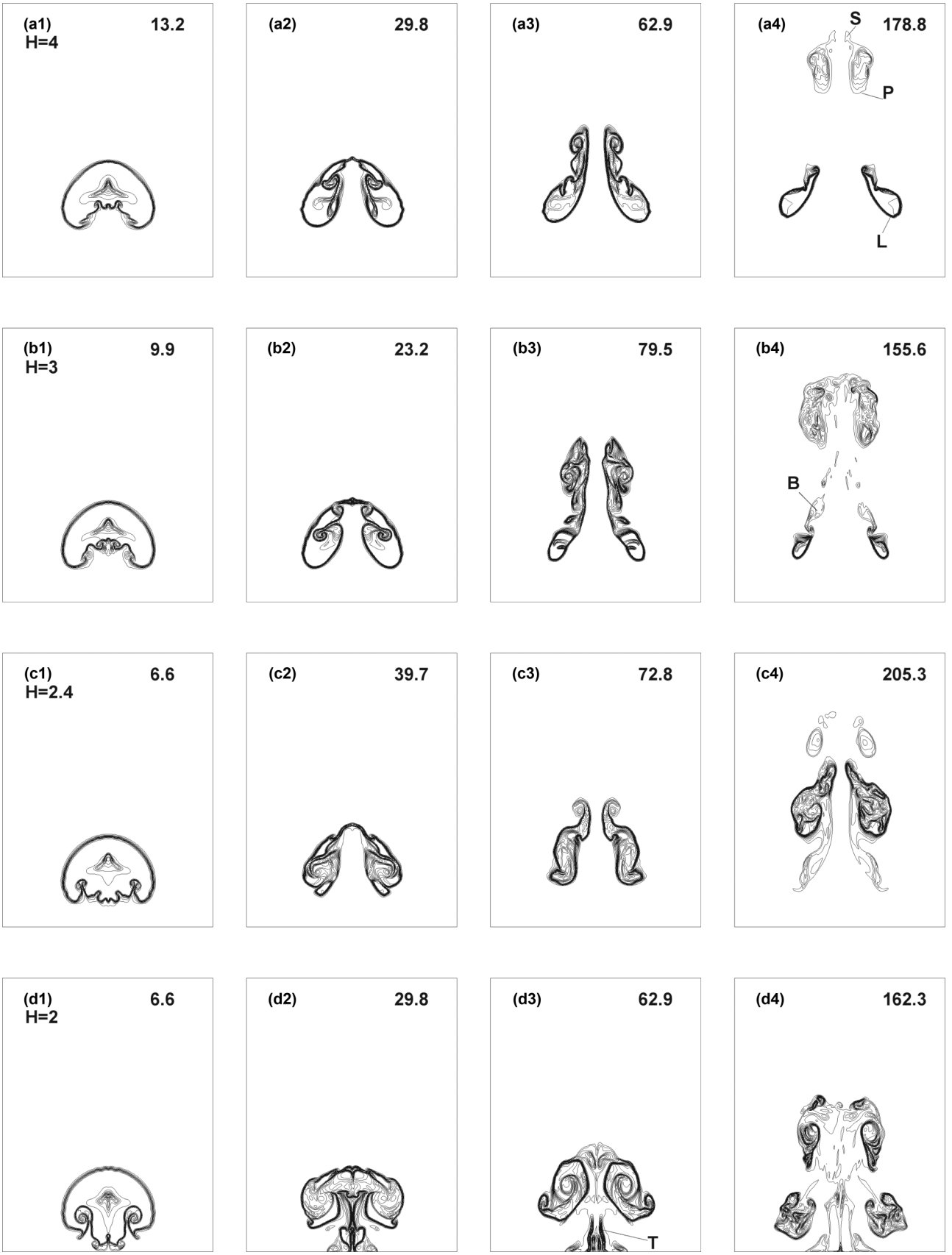

FIG. 8. Isothermal curves depicting the time evolution of the bubble. Rows (a), (b), (c), and (d) correspond to values of H equal to 4, 3, 2.4, and 2, respectively. The time of each plot is indicated at the top right corner. The size of the domain shown is the same in all cases and corresponds to $16r_0$ in height and $12r_0$ in width.

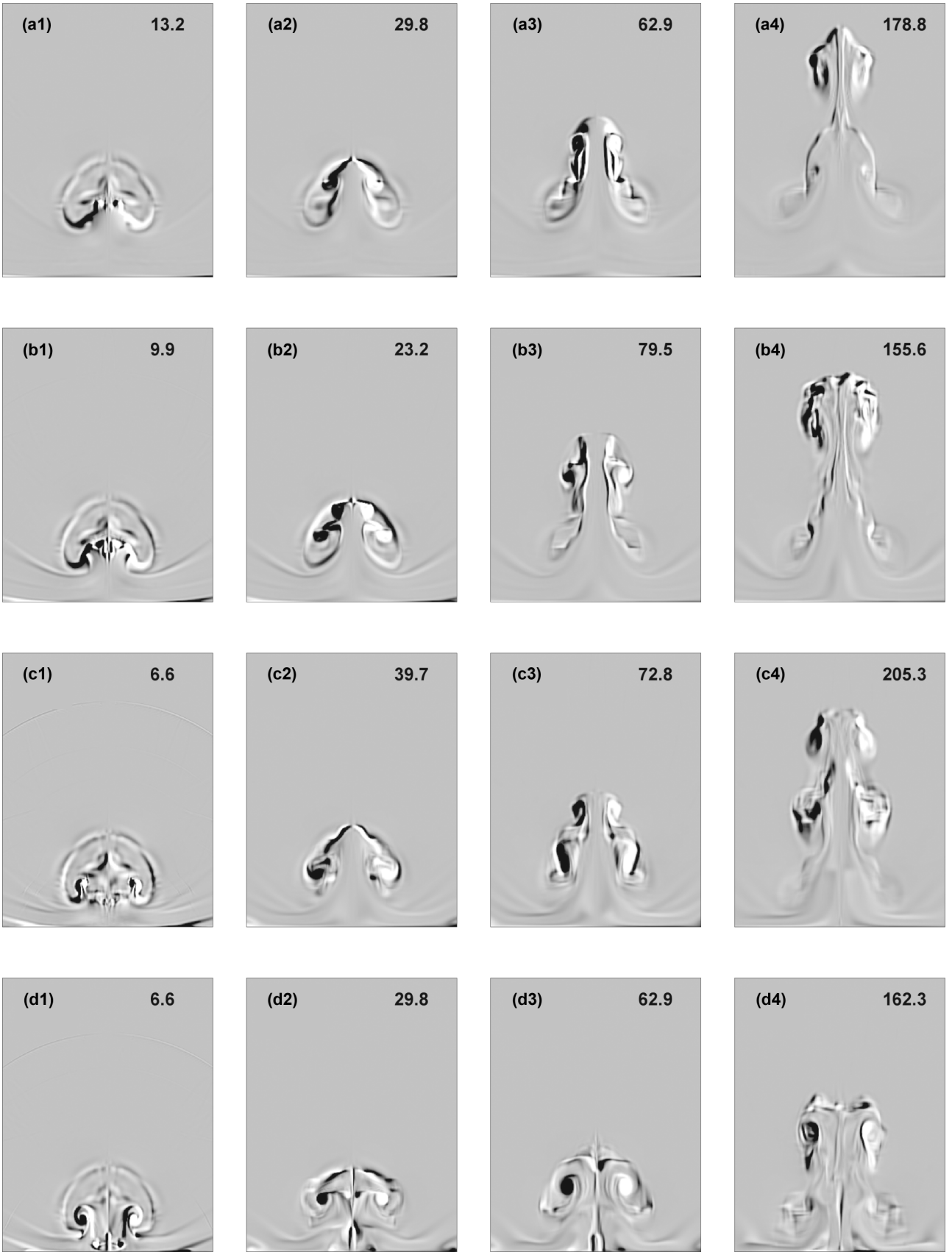

FIG. 9. Component of vorticity in the direction perpendicular to the figures for different times (indicated at the top right corner). Rows (a), (b), (c), and (d) correspond to values of the H equal to 4, 3, 2.4, and 2, respectively. The scales have been skewed to highlight the differences in sign. Domain sizes are the same as in Fig. 8.

of contact between the reflected shock and the interface, the pressure and density gradients are parallel and no vorticity is generated baroclinically. As the interaction progresses the angle of incidence increases and after the transition to an irregular refraction pattern, the generation of vorticity is mainly driven by the transmitted shock [37]. The intensity of the vorticity production then decreases as this wave weakens and becomes increasingly normal to the interface. This results in a vorticity distribution concentrated in the upstream part of the density interfaces, both around the surface and the core of the bubble and with a maximum near the point where the shock refraction ceases to be regular. During the roll-up motion, a secondary vorticity is generated by the vortex accelerated vorticity deposition (VAVD) mechanism described by Peng *et al.* [38] and associated with the centripetal acceleration of the density interfaces. In the downstream hemispheres, this vorticity has opposite sign to that produced by the reflected and transmitted shocks and eventually overtakes it (cf. the first column in Fig. 9).

In simple terms, during the roll-up process, the bubble is stretched and the original upstream part of the density interface moves downstream and takes with it part of the bubble mass, while the downstream part of the interface is driven in the upstream direction and forms the lobe with the rest of the bubble material. Parts of the bubble surface stretched during the roll-up process are found to form the strands connecting the two structures. The resulting vorticity distribution between the primary ring and the lobe then relates to that deposited baroclinically, both by the shocks and the VAVD mechanism, on the upstream and downstream regions of the bubble surface. In our case, because of the presence of the bubble core, the initial generation of vorticity could be depicted as resulting from the interaction of a shock wave with a bubble inside a bubble, making the roll-up process more complex and difficult to describe than the more widely studied case of a uniform inhomogeneity. However, we have been able to follow the evolution of the patches of vorticity during this process and found that those formed on the surface of the bubble are the main source of vorticity for the primary vortex ring, while the vorticity generated near the core is driven downstream by the roll-up motion and ends up mainly in the secondary ring. For $H = 3$ and lower, vorticity of opposite sign is also generated on the two shear layers associated with the triple points in the strong irregular refraction pattern [denoted by C_1 and C_2 in Fig. 5(c)], as can be seen in Figs. 9(b)–9(d). The folding of these layers around the upstream surface of the bubble during the roll-up motion results in an arrangement of three shear layers in close proximity and with vorticity of alternating sign. These regions of high Kelvin-Helmholtz instability are found to increase the entrainment of surrounding gas by the downstream and upstream structures and the irregular strands connecting them [cf. Figs. 8(b4) and 9(b4)].

We now consider in more detail the effect of decreasing H on the vorticity distribution. As the bubble is initialized closer to the boundary, it is reached by the reflected shock at an earlier time and with a higher strength, resulting in a more intense baroclinic deposition of vorticity at the bubble surface and core and a higher circulation in the two downstream vortices. This higher magnitude of vorticity is able to drive more mass from the original bubble into the downstream

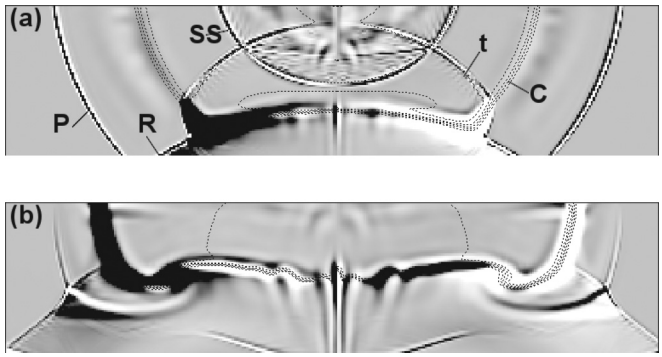

FIG. 10. Distribution of the component of vorticity perpendicular to the figures around the upstream section of the bubble surface: (a) after the interaction with the reflected shock ($\tau = 0.7$) and (b) after the interaction with the second shock ($\tau = 1.2$).

structure, which explains the differences in mass distribution between $H = 4$ and 3. In those two cases the second shock leaves the bubble before it has been reached by the reflected shock and due to the collinearity of the density and pressure gradients, no vorticity is produced baroclinically during this interaction. The situation is different for $H = 2.4$ and 2, as now the reflected shock deforms the bubble surface before the passage of the second shock [Figs. 6(c1) and 6(d1)] and the interaction of the interface with these two waves results in the generation of opposite-signed vorticity. This process can be seen in more detail in Fig. 10 for $H = 2$, where we show the vorticity field around the upstream part of the bubble surface. Clearly visible for $\tau = 0.7$ [Fig. 10(a)] are the second (SS) and transmitted (t) shocks inside the bubble and the distribution of vorticity deposited by the reflected (R) and transmitted shocks on the interface (C). For $\tau = 1.2$ [Fig. 10(b)], the second shock is close to the boundary after being refracted at the bubble surface, which now shows four regions of vorticity with alternating sign. These later bind into the two spikelike structures that can be seen in Figs. 8(c1) and 8(d1) and Figs. 9(c1) and 9(d1). On the left hemisphere of the bubble the vorticity generated by the reflected shock drives the bubble surface to rotate in the counterclockwise direction, while the vorticity generated by the second shock drives this region of the interface towards the boundary. The relative magnitude of these two effects determines the evolution of the surface of the bubble, as the contrast between Figs. 8(c2) and 8(d2) shows. In the case $H = 2.4$, the vorticity generated by the reflected shock dominates and the bubble follows the same roll-up process as for higher H. However, the primary vortex ring now contains similar amounts of opposite-signed vorticity, which results in low circulation and velocity of propagation. The vorticity deposited in the core of the bubble is not affected in the same way by the second shock and this is reflected in the difference in circulation and the larger separation between the two vortex rings [cf. Fig. 8(c4)]. When H is decreased to 2, the strengths not only of the reflected but also of the second shock increase, as the interaction of the latter with the interface occurs closer to the bubble center. The dominant factor in determining the vorticity distribution compared to $H = 2.4$ appears to be the more pronounced deformation of the bubble surface before it is reached by the second shock, as can be seen from Figs. 6(c1)

and 6(d1). After this enlargement of the area of the interface that has been flattened, the vorticity deposited on it by the second shock has enough intensity to cause its separation from the rest of the bubble, forming the stem. This vorticity does not count towards the circulation in the primary vortex ring, which now contains in its core vorticity that is mainly single signed [Fig. 9(d3)], although its circulation is reduced with respect to the cases $H = 4$ and 3.

A further characteristic that can be observed in Fig. 9(d2) is a region between the cores of the primary ring, in which the vorticity has opposite sign to that generated by the reflected and transmitted shocks. We found that this is caused by the flow pattern induced during the formation of the stem and the associated VAVD mechanism. This vorticity is later displaced downstream by the roll-up motion and interacts with the secondary vortex ring, changing the sign of its circulation and causing it to propagate towards the boundary, as described in Sec. IV. It can also be seen in Fig. 9(d2) that in this case the shear layers that originate in the irregular refraction pattern of the strong type remain attached to the stem, thus reducing their effect on the bubble during the roll-up process, and leading to a more coherent vorticity distribution in the core of the primary vortex ring.

To better characterize the changes in the evolution of the bubble in terms of the vorticity field, we calculated the circulation contained in the flow by numerically approximating the surface integral

$$\Gamma_I = \int \omega \, dS, \tag{1}$$

where ω is the azimuthal component of the vorticity and the integration area corresponds to half of the cross sections planes used in the figures, i.e., the regions delimited by the $\hat{x}$ axis, the boundary, and the top and lateral limits of the computational domain. The values of Γ_I were obtained for $\tau = 80$, after the most intense shock waves had left the domain such that their contribution could be neglected [12,39]. For each H, an average value was obtained from measurements taken on eight different planes around the $\hat{x}$ axis and separated by regular angles. The computed values of Γ_I as a function of H are shown in Table I normalized by their value for $H = 4$. It can be seen that there is an increase in circulation between $H = 4$ and 3, which is compatible with the higher intensity of the reflected shock and the enhanced production of vorticity by the baroclinic mechanism. This is also in line with what was found in experimental studies of the standard shock-bubble interaction [35]. However, in contrast to that case, here this trend is eventually reversed as H is reduced because of the generation of opposite-signed vorticity by the second shock, as exemplified by the $H = 2.4$ and 2 cases.

TABLE I. Values of the circulation obtained by integration of the vorticity field Γ_I and using the temporal duration of the roll-up process Γ_T for each H. The measured $\Delta\tau$, L, and W used to calculate Γ_T are also listed.

H	Γ_I	$\Delta\tau$	L	W	Γ_T
4	1	22.7	4.2	5	1
3	1.1	20.7	4	5	1.1
2.4	0.7	37.6	3.7	5	0.5
2	0.1	28.5	3.6	5	0.7

The values of Γ_I are global in the sense that they include the contributions of all the vortical structures in the computational domain, including the stem in the case $H = 2$. To consider only the circulation involved in the creation of the primary vortex ring, we used an alternative approach based on the temporal duration of the roll-up stage. We will assume here that all the dependence on H is contained in the circulation left in the bubble by the time the transmitted shock has crossed the downstream interface. Then the configuration can be described by two characteristic lengths: the bubble height L, in the upstream-downstream direction, and its width W, after it has been compressed by the reflected shock. It has been shown by Yang *et al.* [8] that after a shock-bubble interaction, similarity in the flow structures can be observed in terms of a characteristic time defined by

$$\tau^* = \frac{LW}{\Gamma_T}, \tag{2}$$

where Γ_T is the baroclinically deposited circulation in the bubble. It was described and verified in that work that for different shock strengths and density gradients, the same point in the bubble evolution is observed at the same time, when this is expressed in units of τ^*. Although in our case two vortex rings are formed during this stage, we assume here that the influence of the secondary ring on the roll-up of the bubble can be neglected and that the idea of similarity is still valid.

We measured for each H the time elapsed $\Delta\tau$ between the moment the transmitted shock left the bubble to the point when the upstream part of the bubble surface impinged on the downstream interface. Under the assumption of similarity, the ratio of $\Delta\tau$ for two values of H should be equal to the ratio of the corresponding τ^*. By using (2) and measurements of $\Delta\tau$, L, and W, the ratios of Γ_T to its value for $H = 4$ were estimated and are shown in Table I. While for $H = 3$ and 2.4, the behavior of Γ_T parallels that of Γ_I, the increase in Γ_T for $H = 2$ is an indication that the vorticity generated by the second shock, which leads to a decrease in Γ_I, does not have the same impact on the circulation of the primary vortex ring. As described above, this behavior is caused by the separation of the regions containing vorticity of opposite sign during the formation of the stem. While in the standard shock-bubble problem the circulation in the primary vortex ring increases monotonically with the strength of the shock [35], our results show that for this configuration it has a substantially more complex dependence on the distance H.

VI. CONCLUSION

We have described the early evolution of the low-density inhomogeneity induced in a gas by an instantaneous release of energy near a reflective boundary. We highlighted the qualitative differences between this configuration and the standard shock-bubble interaction problem, mainly in terms of the presence of the ancillary shocks and the nonuniform conditions inside the bubble. We illustrated the changes that occur in the flow structures and vorticity distribution as the distance to the boundary is varied and related those changes

to the baroclinic generation of vorticity by the reflected and second shocks at the bubble surface and core.

We showed four examples that highlight the sensitivity of this process to changes in the offset distance H and it has been explained how these variations relate not only to the strength of the reflected shock but also to the time when this wave reaches the bubble. For $H = 4$ and 3 the interaction of the inhomogeneity with the reflected shock bears similarities to that observed for planar shocks and uniform bubbles, where two main flow structures are formed, a primary vortex ring and an upstream lobe. The amount of circulation and the share of bubble mass contained in the former increase with the strength of the reflected shock and the amount of vorticity it generates, a picture that persists for the cases with $H > 4$ we have looked at. However, we have shown that this trend eventually changes as H is reduced, with the observed decrease in total circulation attributed to the baroclinic production of vorticity by the second shock. This can only occur if the reflected shock deforms the bubble surface prior to its interaction with the second shock and in the case $H = 2.4$ the combination of vorticity of opposite sign originating from each of these two waves results in a significant reduction in the circulation contained in the primary vortex ring. It is worth noting that for $H = 3$ there is a similar interplay between the surface of the bubble and the reflected and third shocks (instead of the second shock), but the rapid decrease in intensity with the increasing order of the ancillary waves results in changes to the circulation and bubble evolution that are substantially weaker. When H is lowered further the diminution in total circulation continues and eventually a point is reached at which the area of the interface where vorticity is generated by the second shock separates from the rest of the bubble, thus reducing its effect on the primary vortex ring. While we have carried out computations for values of H lower than 2, we have found that as the intensities of the multiple wave reflections and ancillary shocks increase, their interactions with the bubble result in very complex vorticity fields at early time. These can only be studied with the substantially higher spatial and temporal resolutions that are beyond the numerical capabilities used for this work.

The existence of ancillary shock waves is a basic property of configurations where energy is introduced in a three-dimensional region during a time that is short relative to the hydrodynamic time scales. In the presence of a boundary and a reflected shock, it can be expected that similar characteristics of the bubble evolution as described here will be observed. In particular, the nonmonotonic variation with H of the circulation contained in the primary vortex ring, which is not observed in the standard shock-bubble problem, relates to the order in which the primary and second shocks interact with the bubble surface. As a result, this will be a generic effect for this type of configuration, although the values of the parameters at which the different transitions occur will vary in each individual case. While in this study we have focused on the early generation of the large-scale vortical structures, at later times, when diffusion and gravitational effects become important, the characteristics of the described vorticity distribution, as well as its sensitivity to the value of H, will have an effect also on the development of small-scale motions and secondary instabilities. Consequently, the processes presented here should be taken into account when considering similar configurations where the amount of circulation and mixing in the flow play an important role.

ACKNOWLEDGMENT

Partial support from the US Department of Energy National Nuclear Security Administration's Offices of Technical Nuclear Forensics and Defense Nuclear Nonproliferation Research and Development is gratefully acknowledged.

[1] J. A. Syage, E. W. Fournier, R. Rianda, and R. B. Cohen, J. Appl. Phys. **64**, 1499 (1988).
[2] G. Taylor, Proc. R. Soc. London Ser. A **201**, 159 (1950).
[3] J. M. Picone, J. P. Boris, J. R. Greig, M. Raleigh, and R. F. Fernsler, J. Atmos. Sci. **38**, 2056 (1981).
[4] J. R. Greig, R. E. Pechacek, and M. Raleigh, Phys. Fluids **28**, 2357 (1985).
[5] H. Sobral, M. Villagrán-Muniz, R. Navarro-González, and A. C. Raga, Appl. Phys. Lett. **77**, 3158 (2000).
[6] H. L. Brode, J. Appl. Phys. **26**, 766 (1955).
[7] J. A. McFadden, J. Appl. Phys. **23**, 1269 (1952).
[8] J. Yang, T. Kubota, and E. E. Zukoski, J. Fluid Mech. **258**, 217 (1994).
[9] J. D. Lindl, R. L. McCrory, and E. M. Campbell, Phys. Today **45**(9), 32 (1992).
[10] D. Ranjan, J. Oakley, and R. Bonazza, Annu. Rev. Fluid Mech. **43**, 117 (2011).
[11] F. J. Berry and M. Holt, Proc. R. Soc. London Ser. A **224**, 236 (1954).
[12] Y. Kurzweil, E. Livne, and B. Meerson, Phys. Fluids **15**, 752 (2003).
[13] Z. Jiang, K. Takayama, K. P. B. Moosad, O. Onodera, and M. Sun, Shock Waves **8**, 337 (1998).
[14] R. J. Leveque, *Finite Volume Methods for Hyperbolic Problems* (Cambridge University Press, New York, 2002).
[15] E. F. Toro, *Riemann Solvers and Numerical Methods for Fluid Dynamics* (Springer, Berlin, 2009).
[16] G. Strang, SIAM J. Numer. Anal. **5**, 506 (1968).
[17] J. H. J. Niederhaus, J. A. Greenough, J. G. Oakley, D. Ranjan, M. H. Anderson, and R. Bonazza, J. Fluid Mech. **594**, 85 (2008).
[18] R. Samtaney and D. I. Pullin, Phys. Fluids **8**, 2650 (1996).
[19] F. Wecken, Z. Math. Mech. **30**, 270 (1950).
[20] M. P. Friedman, J. Fluid Mech. **11**, 1 (1961).
[21] H. L. Brode, Phys. Fluids **2**, 217 (1959).
[22] D. W. Boyer, J. Fluid Mech. **9**, 401 (1960).
[23] I. I. Glass and J. G. Hall, J. Appl. Phys. **28**, 424 (1957).
[24] T. C. J. Hu and I. I. Glass, AIAA J. **24**, 607 (1986).
[25] S. M. Liang, J. S. Wang, and H. Chen, Shock Waves **12**, 59 (2002).
[26] L. F. Henderson, P. Colella, and E. G. Puckett, J. Fluid Mech. **224**, 1 (1991).

[27] A. H. Taub, Phys. Rev. **72**, 51 (1947).
[28] H. Polachek and R. J. Seeger, Phys. Rev. **84**, 922 (1951).
[29] R. G. Jahn, J. Fluid Mech. **1**, 457 (1956).
[30] A. M. A. El Fattah and L. F. Henderson, J. Fluid Mech. **89**, 79 (1978).
[31] J. F. Haas and B. Sturtevant, J. Fluid Mech. **181**, 41 (1987).
[32] J. J. Quirk and S. Karni, J. Fluid Mech. **318**, 129 (1996).
[33] N. K.-R. Kevlahan, J. Fluid Mech. **341**, 371 (1997).
[34] J. M. Picone and J. P. Boris, J. Fluid Mech. **189**, 23 (1988).
[35] D. Ranjan, J. H. J. Niederhaus, J. G. Oakley, M. H. Anderson, R. Bonazza, and J. A. Greenough, Phys. Fluids **20**, 036101 (2008).
[36] G. Layes, G. Jourdan, and L. Houas, Phys. Fluids **21**, 074102 (2009).
[37] R. Samtaney, J. Ray, and N. J. Zabusky, Phys. Fluids **10**, 1217 (1998).
[38] G. Peng, N. J. Zabusky, and S. Zhang, Phys. Fluids **15**, 3730 (2003).
[39] Y. Kurzweil, E. Livne, and B. Meerson, Phys. Fluids **14**, 1030 (2002).